Rational molecular passivation for high-performance perovskite light-emitting diodes

Weidong Xu, Qi Hu, Sai Bai, Chunxiong Bao, Yanfeng Miao, Zhongcheng Yuan, Tetiana Borzda, Alex J. Barker, Elizaveta Tyukalova, Zhang-Jun Hu, Maciej Kawecki, Heyong Wang, Zhibo Yan, Xianjie Liu, Xiaobo Shi, Kajsa Uvdal, Mats Fahlman, Wenjing Zhang, Martial Duchamp, Jun-Ming Liu, Annamaria Petrozza, Jianpu Wang, Li-Min Liu, Wei Huang and Feng Gao

Rational molecular passivation for high-performance perovskite light-emitting diodes

Weidong Xu[1,2], Qi Hu[3], Sai Bai[1], Chunxiong Bao[1,4], Yanfeng Miao[2], Zhongcheng Yuan[1], Tetiana Borzda,[5] Alex J. Barker[5], Elizaveta Tyukalova[6], Zhangjun Hu[1], Maciej Kawecki[7], Heyong Wang[1], Zhibo Yan[1,8], Xianjie Liu[1], Xiaobo Shi[1], Kajsa Uvdal[1], Mats Fahlman[1], Wenjing Zhang[4], Martial Duchamp[6], Jun-Ming Liu[8], Annamaria Petrozza[5], Jianpu Wang[2], Li-Min Liu[9,3]*, Wei Huang[2,10]*, and Feng Gao[1]*

[1]Department of Physics, Chemistry and Biology (IFM), Linköping University, Linköping 58183, Sweden.

[2]Key Laboratory of Flexible Electronics (KLOFE) and Institute of Advanced Materials (IAM), Jiangsu National Synergetic Innovation Center for Advanced Materials (SICAM), Nanjing Tech University (NanjingTech), 30 South Puzhu Road, Nanjing 211816, China.

[3]Beijing Computational Science Research Center, Beijing 100084, China.

[4]International Collaborative Laboratory of 2D Materials for Optoelectronics Science and Technology, Shenzhen University, Shenzhen 518060, China.

[5]Center for Nano Science and Technology @Polimi, Istituto Italiano di Tecnologia, via Giovanni Pascoli 70/3, 20133 Milan, Italy.

[6]School of Materials Science and Engineering, Nanyang Technological University (NTU), 50 Nanyang Avenue, Singapore 639798, Singapore.

[7]Laboratory for Nanoscale Materials Science, Empa, CH-8600 Dubendorf, Switzerland and Department of Physics, University of Basel, CH-4056 Basel, Switzerland.

[8]Laboratory of Solid State Microstructures and Innovation Center of Advanced Microstructures, Nanjing University, Nanjing 210093, P. R. China.

[9]School of Physics, Beihang University, Beijing 1000834, China.

[10]Shaanxi Institute of Flexible Electronics (SIFE), Northwestern Polytechnical University (NPU), 127 West Youyi Road, Xi'an 710072, China.

*Correspondence to: liminliu@buaa.edu.cn (L.M.L.), iamwhuang@nwpu.edu.cn (W.H.), feng.gao@liu.se (F.G.)

Abstract

A major efficiency limit for solution-processed perovskite optoelectronic devices (e.g. light-emitting diodes, LEDs) is trap-mediated non-radiative losses. Defect passivation using organic molecules has been identified as an attractive approach to tackle this issue. However, implementation of this approach has been hindered by a lack of deep understanding of how the molecular structures affect the passivation effectiveness. We show that the so far largely ignored hydrogen bonds play a critical role. By weakening the hydrogen bonding between the passivating functional moieties and the organic cation featuring the perovskite, we significantly enhance the interaction with defects sites and minimize non-radiative recombination losses. Consequently, we achieve exceptionally high-performance near infrared perovskite LEDs (PeLEDs) with a record external quantum efficiency (EQE) of 21.6%. In addition, our passivated PeLEDs maintain a high EQE of 20.1% and a wall-plug efficiency of 11.0% at a high current density of 200 mA cm^{-2}, making them more attractive than the most efficient organic and quantum-dot LEDs at high excitations.

Introduction

Solution-processed metal halide perovskites (MHPs) have received significant interest for cost-effective, high-performance optoelectronic devices[1–4]. In addition to the great successes in photovoltaics (PVs), their excellent luminescence and charge transport properties make them also promising for LEDs[5]. In order to achieve high-efficiency PeLEDs, extensive efforts have been carried out to enhance radiative recombination rates by confining the electrons and holes[6]. These confinement efforts include the use of ultra-thin emissive layers[7], the fabrication of nano-scaled polycrystalline features[8], the design of low-dimensional or multiple quantum well structures[9,10], and the synthesis of perovskite quantum dots[11]. As a result, the EQE values of PeLEDs have improved from less than 1% to ~ 14%[7–11].

In addition to enhancing radiative recombination rates, equally important is to decrease the non-radiative recombination for improving the device performance. Unfortunately, state-of-the-art solution-processed perovskite semiconductors suffer from severe trap-mediated non-radiative losses[12-14], which have been identified as a major efficiency limiting factor for both PVs and LEDs[15,16]. The trap states are generally believed to be associated with ionic defects, such as halide vacancies[17]. Defect passivation through a molecular passivation agent (PA), which can chemically bond with the defects, is an attractive methodology to tackle this issue[18]. A few function groups (e.g. $–NH_2$, P=O) have been identified to passivate perovskite semiconductors for photovoltaic applications[19–21]. It is found that these PAs show strong structure dependent performance, even though they share identical functional groups to interact with the perovskite defects[18–21]. A lack of deep understanding of how the PA chemical structures affect the passivation effects prevents rational design of PAs to minimize the non-radiative recombination losses. These functional groups have also been borrowed to improve the efficiency of LEDs, resulting in limited success so far. For example, the use of trioctylphosphine oxide (TOPO) treatment in green PeLEDs can only result in moderate EQE enhancement from 12% to 14%[22].

Here, we demonstrate high efficiencies for PeLEDs through rational design of passivation molecules. We demonstrate that the candidate amino-functionalized PAs which form stronger hydrogen bonds with organic cations in perovskites are less effective in healing defects sites. Firmly based on our findings, we

design new passivation molecules with decreased hydrogen bonding ability and hence improve their interaction with defects. In particular, we exploit O atoms within the PAs to polarize the passivating amino groups through the inductive effect, reducing their electron-donating ability and hence relevant hydrogen bonding ability. This results in enhanced coordination of the PA functional groups with the perovskite defects sites and hence much improved passivation efficiency. As a result, we are able to substantially decrease the trap-mediated non-radiative recombination and boost the electroluminescence (EL) performance of PeLEDs, giving an average EQE of 19.0 ± 0.8% and a record value of 21.6%.

Results and discussions

PeLED architecture, films characterisations, and device performance

Amino groups have been frequently employed to passivate perovskite semiconductors due to their coordination bonding to unsaturated PbI_6-octahedral[20]. Here, we select two similar amino-functionalized PAs, *i.e.* 2,2′-(ethylenedioxy)diethylamine (EDEA) and hexamethylenediamine (HMDA) (Fig. 1a), which have identical length of alkyl chains; the difference is that EDEA has two additional O atoms within the chain. We perform first-principles calculations to demonstrate that both of them can help to passivate the surface iodide vacancy (V_I) with Pb-N coordination bonding, and thus show the potential to improve the EL performance (Supplementary Figs. 1 and 2). The formamidinium lead tri-iodide ($FAPbI_3$) perovskite layers are deposited by spin-casting the precursors with a molar ratio of PbI_2: formamidinium iodide (FAI): PA = 1: 2: x (x = 0~0.3), where FAI excess is used to eliminate the non-perovskite δ-phase (Supplementary Fig. 3)[23]. We fabricate PeLEDs with the device architecture of indium tin oxide (ITO)/polyethylenimine ethoxylated (PEIE): modified zinc oxide nano-crystals (ZnO:PEIE)/perovskite/poly(9,9-dioctyl-fluorene-co-N-(4-butylphenyl)diphenyl-amine) (TFB)/molybdenum oxide (MoO_3)/Au, as depicted in the high-angle annular dark field cross-sectional scanning transmission electron microscope (HAADF-STEM) images in Fig. 1b. Both HAADF-STEM and scanning electron microscope (SEM) images (Supplementary Fig. 4) show the formation of separated nano-island features in the perovskite emissive layer. These nano-island features have not resulted in strong leakage current (Fig. 1e), possibly due to different TFB thickness on perovskite nano-islands and on ZnO:PEIE as well as unfavourable charge injection from ZnO to TFB

(Supplementary Fig. 5). All the devices show EL peaks at 800 nm/1.55 eV (Fig. 1c) and low turn on voltages around 1.25 V (see Supplementary Fig. 6 for the characterization set-up), where the measurements were performed in a N_2-filled glovebox. In spite of the small difference between the chemical structures of EDEA and HMDA, we notice significant difference in the EQE values of the devices treated with these two PAs (Fig. 1d). The peak EQE is 10.9% for the HMDA-treated devices and 17.9% for the EDEA-treated ones. The EDEA-treated devices show high efficiencies even if we make significant changes to the emissive layer morphologies (Supplementary Figs. 7 and 8), indicating that the difference in the device performance of HMDA- and EDEA-treated devices results from intrinsic different passivation effects of these two PAs.

In order to elucidate the different passivation effects between EDEA and HMDA, we first gather information on the molecular interactions of these moieties with perovskites. The first question that arises is whether these molecules are retained in the perovskite films after the annealing process. We performed time-of-flight secondary ion mass spectrometry (ToF-SIMS) depth profiling (Fig. 1f) and X-ray photoelectron spectroscopy (XPS) characterizations (Supplementary Fig. 9) on perovskite films treated with EDEA, which has the lower boiling point of 105°C and thus represents the most critical sample. By ToF-SIMS we observe the depth distribution of EDEA across the perovskite film by monitoring the unfragmented positive molecular ion ($C_6H_{16}N_2O_2^+$; m = 148.1 u) and by XPS we observe changes in line shape of C1s, O1s, N1s core level spectra in the resulting perovskite films compared to the control ones, confirming the adsorption of EDEA molecules in the perovskite films and thus providing the opportunities for passivation. The passivation through coordination bonding is first evidenced by the strong interaction between PbI_2 and EDEA, leading to a change of the solution colour in their mixture, followed by white precipitation formation (Supplementary Fig. 10). We further performed attenuated total reflectance-Fourier transform infrared (ATR-FT-IR) spectroscopy on the EDEA:PbI_2 mixture. As shown in Fig. 1g, the stretching absorption (ν) bands from the $–NH_2$ of the mixture shift to lower wavenumber with respect to those from the pure EDEA, indicating the formation of coordination bonds between Pb^{2+} and $–NH_2$.

Notably, the molecules used as potential PAs could also be used as templating molecules to synthesize low dimensional perovskites[24,25]. Thus, it is worth to investigate whether these PAs affect the three-

dimensional (3D) crystal structure of $FAPbI_3$. X-ray diffraction (XRD) measurements indicate no additional diffraction peaks other than those from 3D $FAPbI_3$ in the treated perovskite films (Fig. 1h). In addition, no features indicating the presence of Ruddlesden–Popper phases in the ground-state adsorption and photoluminescence (PL) spectra are observed (Supplementary Fig. 11). In order to further confirm the 3D structure in the treated films, we performed transient absorption (TA) spectroscopy (Supplementary Fig. 12) on the control and EDEA-treated films to detect any possible charge transfer kinetics from layered perovskite to the bulk 3D phases, which in principle would present a cascade system in terms of energy levels[26,27]. No additional spectral feature which could be related to low dimensional phases, i.e. of short-lived photobleach, is observed in the treated films, confirming that their photophysics is fundamentally similar to the control samples in this regard.

Passivation mechanism

Assured about the presence of molecular interaction and a lack of structural changes in the thin films, we have investigated the defects physics of the samples. We reveal that the remarkable performance improvement of EDEA-treated PeLEDs origins from the significantly reduced defects in the perovskite emissive layer. Thermal admittance spectroscopy (TAS) was performed to probe the trap density and the energy depth of trap states in the PeLEDs (Fig. 2a). The control and HMDA-treated devices show typical temperature dependent capacitance *vs* frequency (C-f) plots[28,29]. The sub-gap energy deduced from the temperature dependent C-f plots shows a trap energy depth of 0.40 eV and 0.16 eV for the control and HMDA-treated devices, respectively (Supplementary Fig. 13). Fig. 2b and 2c show the trap density deduced from the room temperature C-f plots, giving a peak trap density of 7.8×10^{15} cm^{-3} eV^{-1} and 5.9×10^{15} cm^{-3} eV^{-1} for the control and HMDA-treated devices, respectively. These results indicate a moderate passivation effect of HMDA. In contrast, the EDEA-treated devices show almost temperature independent C-f plots, indicating a negligible influence from trap states and hence excellent passivation.

Excellent defects passivation, which results in significantly reduced trap states in EDEA-treated perovskites, eventually also results in much enhanced external photoluminescence quantum yields (PLQYs) across a large range of excitation fluence, showing a peak PLQY of 56% (Fig. 2d). Even at low fluence of

0.02 mW cm^{-2}, the EDEA-treated films maintain a high PLQY of 40%, consistent with a low defect density. In contrast, the PLQYs of the control and HMDA-treated films show strong intensity dependence due to trap-mediated non-radiative recombination. Low trap-mediated recombination in the EDEA-treated samples is also confirmed by the time-correlated single photon counting (TCSPC) measurements (Fig. 2e), which show a prolonged PL lifetime of 1330 ns compared to the control (130 ns) and HMDA-treated films (690 ns).

The remarkable difference in the passivation effects between EDEA and HMDA indicates the significance of O atoms in EDEA for efficient passivation. A straightforward possibility for the O atoms to affect the passivation is that the two pairs of lone pair electrons at the O atom in EDEA can coordinate with Pb^{2+} and hence passivate the defects. In order to examine this possibility, we employed ethylene glycol diethyl ether (EGDE) as the PA molecule (Supplementary Fig. 14). The only difference between EGDE and EDEA is that the former does not contain amino groups. Compared with the control samples, we observe no improvement on the PL properties as well as the device performance in the EGDE-treated ones (Supplementary Fig. 14), indicating no passivation effects of EGDE. Our first-principle calculations confirm that the O atom in EGDE cannot effectively passivate $FAPbI_3$ for the following two reasons: 1, the O atoms lie in the middle of the molecule chain of EGDE, causing strong lattice distortion energy when coordinated with Pb^{2+}; 2, the molecular dynamics show that even if the O atom initially bonds with Pb^{2+}, the coordination bonds could be quickly broken to form hydrogen bonds between O and FA^+, destroying the passivation effects.

Having excluded direct passivation mechanisms through the O atom, we proceed to investigate other reasons for the different passivation effectiveness between EDEA and HMDA. We notice that there are strong intermolecular interactions between FAI and PAs, resulting in the formation of gel-like mixtures (Supplementary Fig. 15a). The ATR-FT-IR spectra (Fig. 3a) show obvious broadened absorption from ν(N–H) and ν(C–H) of the EDEA/FAI mixture compared to those in pure FAI and EDEA. In addition, the N–H scissoring vibration (δ(N–H)) absorption bands greatly weakens in the mixture, suggesting the restriction of the N–H bending caused by intermolecular interactions. A similar phenomenon is also observed in the

ATR-FT-IR spectra of HMDA/FAI mixture (Supplementary Fig. 15b). All these results confirm the formation of hydrogen bonds between PAs and FAI[30,31].

Since both hydrogen bonds and passivating coordination bonds result from the lone pair electrons at the N atoms in the amino groups, changes in the hydrogen bonding ability will affect the passivation effect. Importantly, the hydrogen bonds between the amino groups and FA^+ can be affected by the O atom because of the electron withdrawing inductive effect of O atoms. Fig. 3b shows the electron distributions of the EDEA and HMDA. Compared with HMDA, the electrons at the N atoms of EDEA polarize toward the O atoms due to the inductive effects, which hence reduce the electron-donating ability of the amino groups and the relevant hydrogen bonding ability[33]. The stronger hydrogen bonding ability of HMDA is first evidenced by its higher melting point (43°C) compared to EDEA (liquid at room temperature) due to the enhanced intermolecular interaction. We further confirm that hydrogen bonding abilities of EDEA and HMDA with FAI are different by using ^{1}H nuclear magnetic resonance (^{1}H NMR) measurements. Generally, strong hydrogen bonding causes large chemical shifts to low-field (high p.p.m.) because of de-shielding. As shown in Fig. 3c, the proton chemical shift at 8.9 ppm from pure FAI corresponds to the resonance from the active protons at its amino groups[20]. This peak is broadened and moves to 7.7 ppm and 5.9 ppm with the introduction of 15% HMDA and EDEA, respectively. These results not only confirm the formation of new hydrogen bonds for both PA molecules, but also demonstrate weaker hydrogen bonding ability of EDEA with respect to HMDA.

In order to quantify how the hydrogen bonds affect the passivation mechanism, we investigate the adsorption configurations of the PAs on a perfect 110 $FAPbI_3$ slab (Fig. 3d and 3f) and on a defect-contained surface (iodide vacancy, V_I) (Fig. 3e and 3g) by first-principles calculations. The adsorption energy difference (ΔE_{ad}) between these two surfaces is calculated to probe the preferred PA adsorption location, and hence to quantify the competition between the passivation and hydrogen bonding. The adsorption energy on the perfect surface ($E_{ad,P}$) is determined by Van der Waals interaction and the hydrogen bonds (between FA^+ and all the electron rich groups (N, O)). As a result of the inductive effect, we find the decrease of absolute $E_{ad,P}$ value of EDEA, even considering that its O atoms can provide an additional

hydrogen bond with FA^+ (Fig. 3f). This result is consistent with the ^1H NMR measurements that HMDA shows stronger hydrogen bonding with FA^+. For the surface with V_I, coordination bonds also contribute to the adsorption energy ($E_{ad,V}$) in addition to hydrogen bonding and Van der Waals interaction. The ΔE_{ad} is then determined by $\Delta E_{ad} = E_{ad,V} - E_{ad,P}$. Negative ΔE_{ad} values indicate a preferred interaction with the defect-contained structure through coordination bonds; while positive ΔE_{ad} values indicate a preferred interaction with the perfect perovskite surface through hydrogen bonds. The ΔE_{ad} for EDEA is -0.23 eV and that for HMDA is 0.45 eV, indicating that it is much easier for EDEA to break down the hydrogen bonds and turn to work with defects. The significant difference of the ΔE_{ad} values between EDEA and HMDA explains the remarkable effect of O atoms in manipulating the passivation effects. An additional advantage of the O atom in EDEA is that it might help to improve the stability. The extra hydrogen bonds provided by the O atoms can stabilize the rotating FA^+ (Fig. 3f) and hence mitigate the negative effects from the thermal vibration and the relevant lattice distortion (as shown in HMDA adsorbed structure, Fig. 3d). In reality the PA/perovskites interactions could be much more complex, involving Van der Waals and hydrogen bonding between neighbouring surface modifiers, regardless, the experimental data confirm that EDEA is more effective at reducing non-radiative recombination.

The dependence of PeLEDs performance on the passivation effectiveness

Having established the role that the O atom plays in affecting the passivation effects, we proceed to explore new PAs, aiming to both further validate our conclusions and improve the device performance. We designed three PAs (Fig. 4a) with different strength of inductive effects, which are expected to result in different hydrogen bonding abilities and hence different passivation effectiveness. Compared with EDEA, the inductive effect can be increased by introducing one additional O atom (as in 2,2′-[oxybis(ethylenoxy)]diethylamine (ODEA)), and reduced by increasing the length of alkyl chain between the N and O atoms (as in 4,9-dioxa-1,12-dodecanediamine (DDDA) and 4,7,10-trioxa-1,13-tridecanediamine (TTDDA))[33]. Among all the PAs with O atoms, the inductive effect in DDDA is the least effective since its N and O atoms are almost isolated from each other, resulting in the strongest hydrogen bonding ability of the amino groups. The morphological and optical characterizations for each PA

passivated perovskite films are shown in Supplementary Figs. 16 and 17. The adsorption configurations and E_{ad} values are depicted in Supplementary Fig. 18 and summarized in Supplementary Table 1. Fig. 4b shows the average peak EQE values for all the passivated systems as a function of ΔE_{ad} (see represented device characteristics in Supplementary Figs. 19 and 20). It clearly shows that the EL performance is strongly dependent on the $\Delta E_{ad,}$ and hence the hydrogen bonding ability of amino groups. As expected, ODEA, which shows a ΔE_{ad} value of -0.42 eV, delivers the highest average peak EQE of 19.0 ± 0.8% (Fig. 4b-c and Supplementary Fig. 21). The excellent passivation effects of the ODEA are also confirmed by the fluence-dependent PLQY measurements and TAS measurements (Supplementary Fig. 22).

We show the characteristics for the best performing ODEA-treated device, which gives a peak EQE up to 21.6% (Fig. 4e), approaching the best organic and quantum dot LEDs[34,35]. The radiance rapidly rises after the device turns on, reaching a high radiance of 308 W Sr^{-1} m^{-2} at 3.3 V (Fig. 4d). The high EQE and low driving voltage result in an exceptionally high peak wall-plug efficiency up to 15.8% (Fig. 4e). High efficiencies at high current densities have been challenging in other low-temperature processed LED techniques (e.g. organic LEDs) due to low charge carrier mobilites and strong exciton-induced quenching effects. Our device exhibits a low efficiency roll-off, maintaining a high EQE of 20.1 % and a wall-plug efficiency of 11.0% at a high current density of 200 mA cm^{-2}, which makes them much more efficient than OLEDs and QLEDs at high excitations[34,35]. We also tested the operation lifetime (T_{50}, time to half of the initial radiance) of these devices in the glovebox without encapsulation. The ODEA-treated devices are among the most stable PeLEDs to date[8–11,22,36], showing a long lifetime of 20 h at 25 mA cm^{-2} compared with the control devices (T_{50} = 1.5 h at 25 mA cm^{-2}) (Fig. 4f). The improved lifetime may result from the reduced Joule heating due to the high efficiency, or the suppression of ion migration due to the low defect density[12,37]. We also notice a rapid degradation at high current densities (T_{50} =18 min at 200 mA cm^{-2}) (Supplementary Fig. 23). Future research on the degradation mechanisms, especially at high current densities, will be of key importance to practical applications of PeLEDs.

Conclusions

In summary, we have demonstrated high-efficiency near infrared PeLEDs with a peak EQE of 21.6%, which represents the most efficient PeLEDs to date. Our devices also show low efficiency roll-off, maintaining a high EQE of 20.1% and a wall-plug efficiency of 11.0% at a high current density of 200 mA cm^{-2}. Our results indicate a unique opportunity for PeLEDs to achieve solution processed large-scaled LEDs with high efficiencies at high brightness. The high efficiencies stem from our deep understanding of the passivation mechanisms of perovskites by organic molecules. We reveal the critical role of hydrogen bonds in affecting the passivation effectiveness. By weakening the hydrogen bonding between the passivating functional groups and the organic cations of perovskites, we significantly reduce the non-radiative recombination. Our findings provide a broad avenue to explore the potential of molecular passivation for improving various perovskite applications where non-radiative losses should be minimized.

Acknowledgements

We thank T.C. Sum, S.S. Lim, J. Zhang, W. Tress, W. Chen, Y. Puttisong, Y.T. Gong, C.Y. Kuang, and C. Deibel for useful discussions. This work is supported by the ERC Starting Grant (717026), the National Basic Research Program of China (973 Program, grant number 2015CB932200), the National Natural Science Foundation of China (61704077, 51572016, 51721001 and U1530401), the Natural Science Foundation of Jiangsu Province (BK20171007), the National Key Research and Development Program of China Grant No. 2016YFB0700700, the European Commission Marie Skłodowska-Curie Actions (691210), Swiss National Science Foundation (CR23I2-162828), Nanyang Technological University start-up grant M4081924, and the Swedish Government Strategic Research Area in Materials Science on Functional Materials at Linköping University (Faculty Grant SFO-Mat-LiU no. 2009-00971). The TEM measurements were performed at the Facility for Analysis, Characterization, Testing and Simulation (FACTS) in Nanyang Technological University, Singapore. W.X. is a Wenner-Gren Postdoc Fellow; F.G. is a Wallenberg Academy Fellow.

Author Contributions

F.G. and W.X. conceived the idea and designed the experiments; W.X. performed the experiments and analysed the data; F.G. and W.H. supervised W.X.; Q.H. performed first-principle calculations on the molecular passivation under the supervision of L.M.L; Y.M., Z.Y., H.W. X.S. and Z.Y. contributed to device fabrication and measurements; Y.M. performed fluence dependent PLQY and TCSPC measurements and analysed the data under the supervision of J.W. and W.H.; Y.M. and J.W. cross-checked the device performance at Nanjing Tech University; S.B. and Z.Y. synthesized and modified the ZnO nano-crystal and contributed to the device development; C.B. performed the TAS measurements and analysed the data; Z.H. performed the FT-IR measurements and analysed the data; X.L. performed XPS tests and analysed the data; E.T. performed the STEM tests under the supervision of M.D.; T.B. and A.J.B. performed the transient absorption measurements and analysed the data under the supervision of A.P.; M.K. performed the TOF-SIMS measurements and analysed the data; J.L., M.F., K.U. and W.Z. contributed to the data

analysis; W.X. and F.G. wrote the manuscript; S.B., J.W. and A.P. provided revisions to the manuscript; F.G. supervised the project; All authors discussed the results and commented on the manuscript.

Additional information

Supplementary information is available in the online version of the paper. Correspondence to L.L. W. H. and F.G..

Data availability

The data that support the plots within this paper and other findings of this study are available from the corresponding author upon reasonable request.

Competing interests

F.G. and W.X. have filed a patent application related to this work.

References

1. Tan, Z.-K. *et al.* Bright light-emitting diodes based on organometal halide perovskite. *Nat. Nanotechnol.* **9,** 687–692 (2014).
2. Akkerman, Q. A. *et al.* Strongly emissive perovskite nanocrystal inks for high-voltage solar cells. *Nat. Energy* **2,** 16194 (2017).
3. Dou, L. *et al.* Solution-processed hybrid perovskite photodetectors with high detectivity. *Nat. Commun.* **5,** 5404 (2014).
4. Shi, X. *et al.* Optical energy losses in organic-inorganic hybrid perovskite light-emitting diodes. *Adv. Opt. Mater.* **6,** 1800667 (2018).
5. Stranks, S. D. & Snaith, H. J. Metal-halide perovskites for photovoltaic and light-emitting devices. *Nat. Nanotechnol.* **10,** 391–402 (2015).
6. Xing, G. *et al.* Transcending the slow bimolecular recombination in lead-halide perovskites for electroluminescence. *Nat. Commun.* **8,** 14558 (2017).
7. Li, G. *et al.* Efficient light-emitting diodes based on nanocrystalline perovskite in a dielectric

polymer matrix. *Nano Lett.* **15,** 2640–2644 (2015).

8. Xiao, Z. *et al.* Efficient perovskite light-emitting diodes featuring nanometre-sized crystallites. *Nat. Photonics* **11,** 108–115 (2017).
9. Wang, N. *et al.* Perovskite light-emitting diodes based on solution-processed self-organized multiple quantum wells. *Nat. Photonics* **10,** 699–704 (2016).
10. Zou, W. *et al.* Minimising efficiency roll-off in high-brightness perovskite light-emitting diodes. *Nat. Commun.* **9,** 608 (2018).
11. Li, G. *et al.* Surface ligand engineering for near-unity quantum yield inorganic halide perovskite QDs and high-performance QLEDs. *Chem. Mater.* **30,** 6099–6107(2018).
12. Abdi-Jalebi, M. *et al.* Maximizing and stabilizing luminescence from halide perovskites with potassium passivation. *Nature* **555,** 497–501 (2018).
13. Stranks, S. D. Nonradiative losses in metal halide perovskites. *ACS Energy Lett.* **2,** 1515–1525 (2017).
14. Tress, W. Perovskite solar cells on the way to their radiative efficiency limit – insights into a success story of high open-circuit voltage and low recombination. *Adv. Energy Mater.* **7,** 1602358 (2017).
15. Correa-Baena, J.-P. *et al.* Promises and challenges of perovskite solar cells. *Science* **358,** 739–744 (2017).
16. Braly, I. L. *et al.* Hybrid perovskite films approaching the radiative limit with over 90% photoluminescence quantum efficiency. *Nat. Photonics* **12,** 355–361 (2018).
17. Agiorgousis, M. L., Sun, Y. Y., Zeng, H. & Zhang, S. Strong covalency-induced recombination centers in perovskite solar cell material $CH_3NH_3PbI_3$. *J. Am. Chem. Soc.* **136,** 14570–14575 (2014).
18. Noel, N. K. *et al.* Enhanced photoluminescence and solar cell performance via Lewis base passivation of organic-inorganic lead halide perovskites. *ACS Nano* **8,** 9815–9821 (2014).
19. Dequilettes, D. W. *et al.* Photoluminescence lifetimes exceeding 8 μs and quantum yields exceeding 30% in hybrid perovskite thin films by ligand passivation. *ACS Energy Lett.* **1,** 438–444

(2016).

20. Wang, F. *et al.* Phenylalkylamine passivation of organolead halide perovskites enabling high-efficiency and air-stable photovoltaic cells. *Adv. Mater.* **28,** 9986–9992 (2016).

21. Zheng, X. *et al.* Defect passivation in hybrid perovskite solar cells using quaternary ammonium halide anions and cations. *Nat. Energy* **2,** 17102 (2017).

22. Yang, X. *et al.* Efficient green light-emitting diodes based on quasi-two-dimensional composition and phase engineered perovskite with surface passivation. *Nat. Commun.* **9,** 570 (2018).

23. Ma, F. *et al.* Stable α/δ phase junction of formamidinium lead iodide perovskites for enhanced near-infrared emission. *Chem. Sci.* **8,** 800–805 (2016).

24. Cortecchia, D. *et al.* Broadband emission in two-dimensional hybrid perovskites: The role of structural deformation. *J. Am. Chem. Soc.* **139,** 39–42 (2017).

25. Chen, Z. *et al.* High-performance color-tunable perovskite light emitting devices through structural modulation from bulk to layered film. *Adv. Mater.* **29,** 1603157 (2017).

26. Neutzner, S., Srimath Kandada, A. R., Lanzani, G. & Petrozza, A. A dual-phase architecture for efficient amplified spontaneous emission in lead iodide perovskites. *J. Mater. Chem. C* **4,** 4630–4633 (2016).

27. Yuan, M. *et al.* Perovskite energy funnels for efficient light-emitting diodes. *Nat. Nanotechnol.* **11,** 872–877 (2016).

28. Duan, H. S. *et al.* The identification and characterization of defect states in hybrid organic-inorganic perovskite photovoltaics. *Phys. Chem. Chem. Phys.* **17,** 112–116 (2015).

29. Bi, C. *et al.* Non-wetting surface-driven high-aspect-ratio crystalline grain growth for efficient hybrid perovskite solar cells. *Nat. Commun.* **6,** 7747 (2015).

30. Dai, H. *et al.* A temperature-responsive copolymer hydrogel in controlled drug delivery. *Macromolecules* **39,** 6584–6589 (2006).

31. Chen, H. *et al.* A solvent-and vacuum-free route to large-area perovskite films for efficient solar modules. *Nature* **550,** 92–95 (2017).

32. Taylor, V. C. A. *et al.* Investigating the role of the organic cation in formamidinium lead iodide

perovskite using ultrafast spectroscopy. *J. Phys. Chem. Lett.* **9,** 895–901 (2018).

33. Gero, A. Inductive effect and hydrogen bonding as factors in the base strength of polymethylenediamines. *J. Am. Chem. Soc.* **76,** 5159–5160 (1954).

34. Dai, X. *et al.* Solution-processed, high-performance light-emitting diodes based on quantum dots. *Nature* **515,** 96–99 (2014).

35. Ly, K. T. *et al.* Near-infrared organic light-emitting diodes with very high external quantum efficiency and radiance. *Nat. Photonics* **11,** 63–68 (2016).

36. Cao, Y. et al. Perovskite light-emitting diodes based on spontaneously formed submicrometre-scale structures. *Nature* **562**, 249−253 (2018).

37. Xiao, X. et al. Suppressed ion migration along the in-plane. *ACS Energy Lett.* **3**, 684−688 (2018).

The figure legends

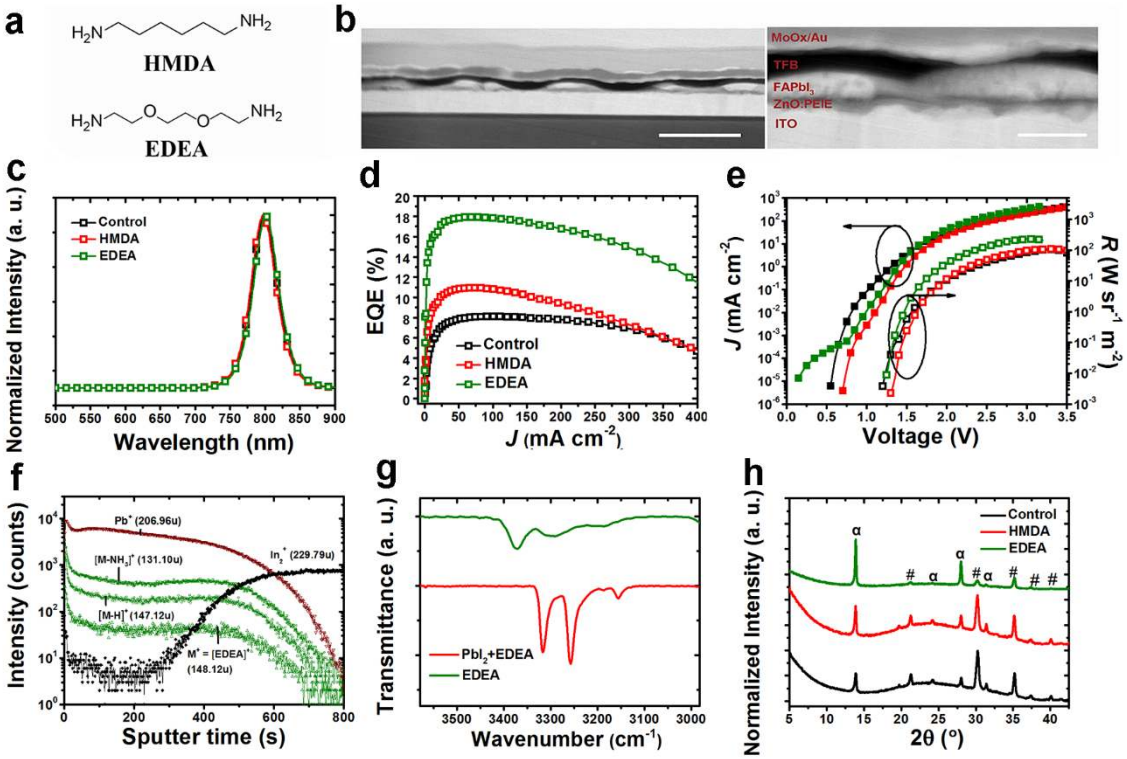

Figure 1 | PeLED architecture, performance and perovskite film characteristics. a, The molecular structures of HMDA and EDEA. **b**, A HAADF cross-sectional image of an EDEA-treated device (left, scale bar 500 nm) and a zoom-in image (right, scale bar 100 nm). Represented characteristics for the optimized control, EDEA- and HMDA-treated devices: **c**, EL spectra at 2.5 V; **d**, *EQE-J* curves; **e**, Current density-voltage-radiance (*J-V-R*) characteristics. **f**, TOF-SIMS for the 0.25 EDEA-treated perovskite film on the ITO/ZnO:PEIE substrate, showing depth profiles of unfragmented EDEA (M^+= $EDEA^+$) and two characteristic fragment ions ($[M\text{-}NH_3]^+$ and $[M\text{-}H]^+$). **g**, ATR-FT-IR (N-H stretching) for EDEA and PbI_2:EDEA mixture. **h**, XRD patterns for the control, EDEA- ($x = 0.25$) and HMDA-treated ($x = 0.25$) films on the ITO/ZnO:PEIE substrates. α and # denote the diffraction peaks corresponding to α-$FAPbI_3$ and ITO, respectively.

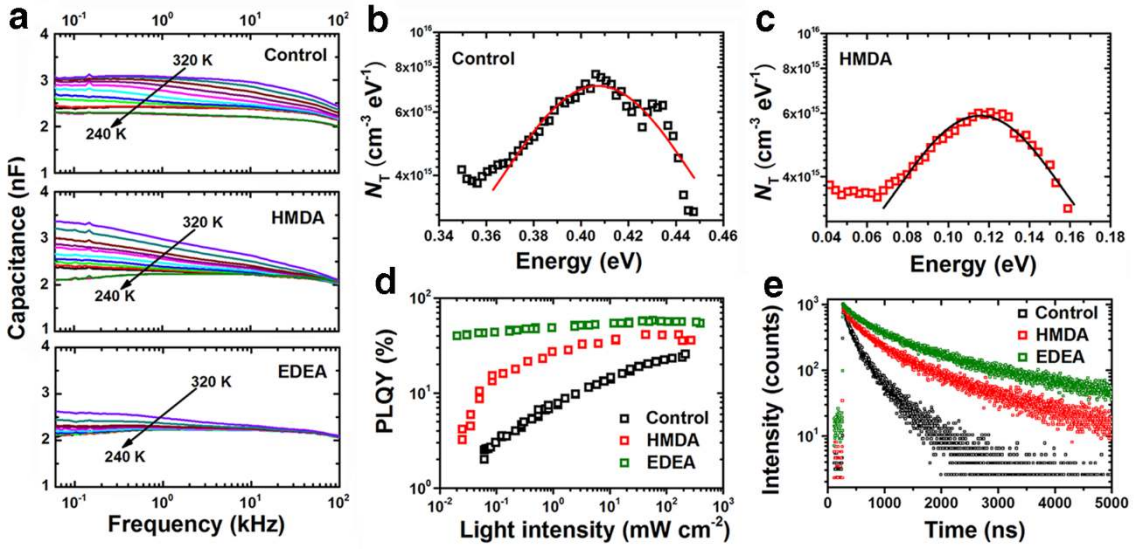

Figure 2 | The evidence for the excellent passivation effects of EDEA treatment. **a**, Temperature dependence of capacitance-frequency plots for control, HMDA-treated and EDEA-treated devices (from 320 ~ 240 K). **b**, **c**, Trap density deduced from the room temperature C-f plots for the control (**b**) and the HMDA-treated (c) samples. **d**, Fluence-dependent PLQYs. **e**, Time-correlated single photon counting (TCSPC) probed PL lifetime. The excitation density for the TCSPC measurement is around 10^{15} cm^{-3}.

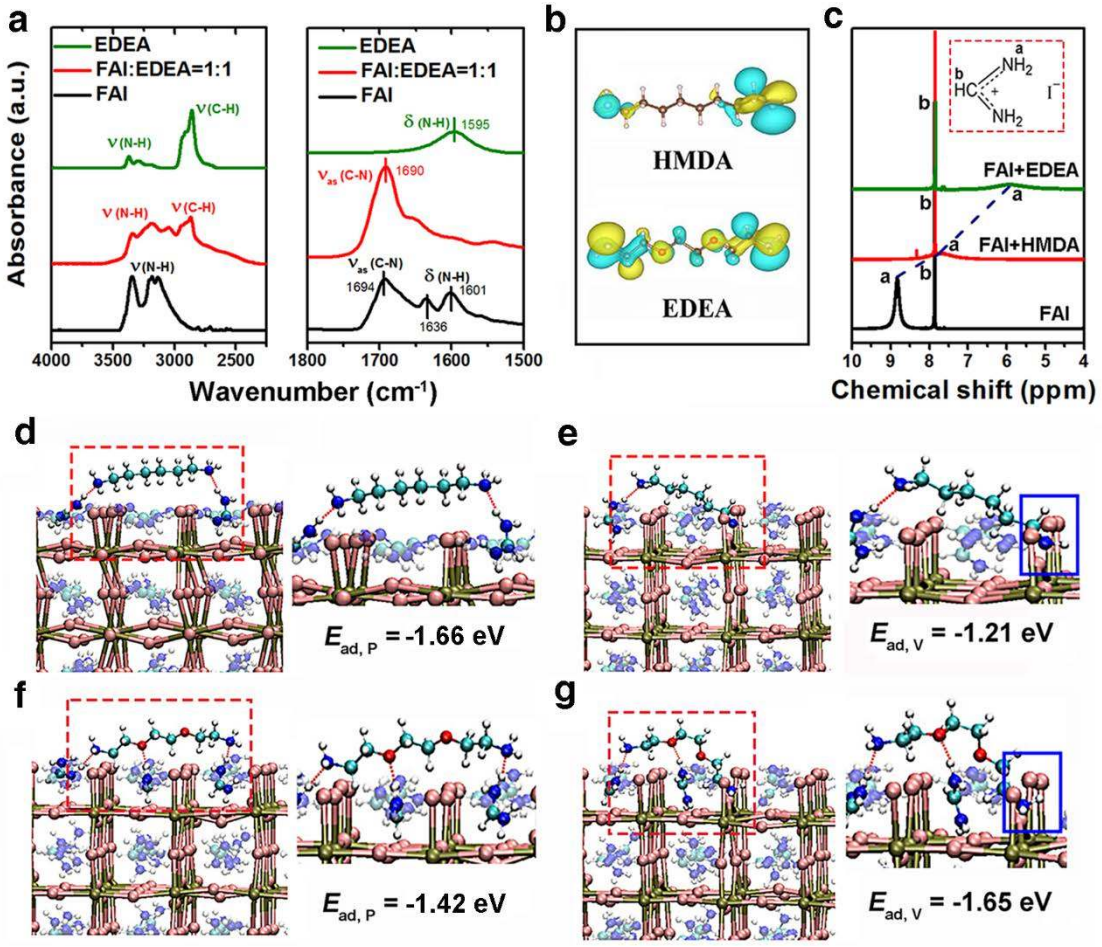

Figure 3 | Understanding how the hydrogen bonds affect the passivation effects. a, The ATR-FT-IR spectra of FAI, EDEA and FAI:EDEA (1:1) mixture. ν_{as}(C–N) denotes the C–N antisymmetric stretching vibration from FAI[32]. **b**, Calculated electron distribution (VBM) of HMDA and EDEA. **c**, ^{1}H NMR spectra of the FAI in DMSO and FAI with 15% EDEA or HMDA addition. Peaks *a* and *b* are the characteristic of H (a) and H (b) as labelled in the molecular structure of FAI. (**d**-**g**) Adsorption configurations of HMDA (**d**, **e**) and EDEA (**f**, **g**) on perfect $FAPbI_3$ 110 slab (**d**, **f**) and on defect-contained structure (**e**, **g**). The red, blue, cyan and white spheres represent O, N, C, H atoms, respectively. The hydrogen and coordination bonds are denoted by red dotted lines and blue squares, respectively.

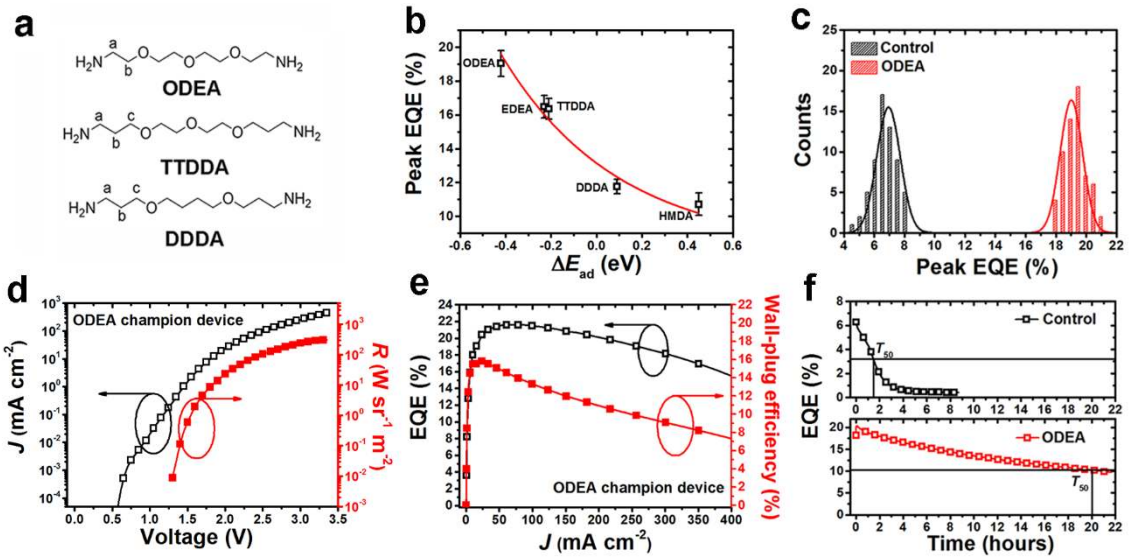

Figure 4 | The dependence of EL performance on passivation effects determined by the hydrogen bonds. a, The molecular structures of selected PAs (ODEA, TTDDA, DDDA). The letters shown in the chemical structures aim to highlight the different length of carbon chain between N and O atoms. **b**, Dependence of average peak EQE values from various PAs treated PeLEDs on ΔE_{ad}. Each value is an average of 60 devices. **c**, Histograms of peak EQEs for control and ODEA-treated devices. Device characteristics for the best performing ODEA-treated device: **d**, *J*-*V*-*R* characteristics; **e**, EQE and Wall-plug efficiency as a function of the current density; **f**, Steady-state EQE for the control and ODEA-treated devices at 25 mA cm^{-2}. We select the maximum EQE as the initial value for the calculation of T_{50}. The device shown in d-f was fabricated from a different batch of ZnO nano-crystals, and hence not included in the statistics of b-c.

Methods

Materials. The passivation agents (PAs), including hexamethylenediamine (HMDA), 2,2′-(ethylenedioxy)diethylamine (EDEA), 4,9-dioxa-1,12-dodecanediamine (DDDA), 2,2′-[oxybis(ethylenoxy)]diethylamine (ODEA), 4,7,10-trioxa-1,13-tridecanediamine (TTDDA), ethylene glycol diethyl ether (EGDE) were purchased from Sigma-Aldrich. Formamidinium iodide (FAI) was purchased from Dyesol. PbI_2 (beads, 99.999%) was purchased from Alfa Aesar. Poly(9,9-dioctyl-fluorene-co-N-(4-butylphenyl)diphenylamine) (TFB) was purchased from Ossila. Other materials for device fabrication were all purchased from Sigma-Aldrich.

Preparation of the perovskite solution. Perovskite precursors (FAI: PbI_2: PA molar ratio of 2: 1: x, x = 0 ~ 0.3) were prepared with dimethylformamide (DMF) as the solvent. A 10 mg mL^{-1} PA solution was prepared at first, and then was diluted according to the required molar ratio to Pb^{2+}. The optimal concentration for PbI_2 was 0.13 M. The solution precursors were stirred at 50˚C for 12 h before spin-coating. Colloidal ZnO nanocrystal was synthesized by a solution–precipitation process, and the details can be found in the literature[38].

PeLED fabrication. The indium tin oxide (ITO) glass substrates were sequentially cleaned by detergent and TL-1 (a mixture of water, ammonia (25%), and hydrogen peroxide (28%) (5:1:1 by volume)). The clean substrates were then treated by UV-ozone for 10 min. The ZnO nanocrystal solutions were spin-casted onto the substrates at 4,000 rpm for 30 s in air. Then the substrates were moved into a N_2-filled glovebox. Next, a layer of polyethylenimine ethoxylated (PEIE) was deposited at 5,000 rpm (0.05 wt%, in IPA), followed by annealing at 100°C for 10 min. After cooling down to room temperature, the perovskite films were deposited from the precursors with various PA contents and Pb^{2+} concentrations at a spin-coating speed of 3,000 rpm, followed by annealing at 100°C for 10 min. For the control perovskite films prepared by anti-solvent treatment, the spin-casting rate is 5,000 rpm. In addition, 150 μL chlorobenzene (CB) was dropped after 5 seconds spinning. The TFB layer was deposited from its CB solution (12 mg mL^{-1}) at 3,000 rpm. Finally, the MoO_x/Au electrode was deposited by a thermal

evaporation system through a shadow mask under a base pressure of ~1×10^{-7} torr. The device area was 7.25 mm^{-2} as defined by the overlapping area of the ITO films and top electrodes.

PeLEDs characterization. All PeLED device characterizations were carried out at room temperature in a nitrogen-filled glovebox. A Keithley 2400 source meter and a fibre integration sphere (FOIS-1) coupled with a QE Pro spectrometer (Ocean Optics) was used for the measurements. The PeLED devices are tested on top of the integration sphere and only forward light emission can be collected, consistent with the standard OLED characterization method. The absolute radiance was calibrated by a standard Vis-NIR light source (HL-3P-INT-CAL plus, Ocean Optics). The devices were swept from zero bias to forward bias. The time evolution of the EQE was measured using the same testing system. To verify the accuracy of our characterization set-up, we crosschecked our results at Nanjing Tech University. The performance obtained in the two laboratories are in good agreement (Supplementary Table 2).

First-Principles Calculations. We used the CP2K/Quickstep package to carry out the first principles calculations. The exchange correlation energy was described with the Generalized Gradient Approximation (GGA) of Perdew-Burke–Ernzerhof (PBE)[39]. The norm-conserving Goedecker-Teter-Hutter (GTH) pseudopotentials was used to describe the core electrons[40]. Gaussian function with molecularly optimized double-zeta polarized basis sets (m-DZVP) were adopted for expanding the wave function of Pb $6s^26p^2$, I $5s^25p^5$, H $1s^2$, C $2s^22p^2$, O $2s^22p^4$ and N $2s^22p^3$ electrons[41]. The auxiliary basis set of plane waves was set as 500 Ry cut-off energy. We modelled the $FAPbI_3$ (110) surface as a 2 layers slab with a 2×2 surface supercell (25.74×25.13 Å). We used a vacuum of 15 Å to separate images along the surface normal direction.

The adsorption energies were calculated with the following equation:

$$E_{ad} = E_{adsorbed} - E_{decoupled} \quad (1)$$

Here, the $E_{adsorbed}$ is the energy of the adsorption configuration, while $E_{decoupled}$ is the energy of the decoupled system, including the clean system and the single molecule.

Perovskite film characterizations. X-ray diffraction patterns were obtained from an X-ray diffractometer (Panalytical X'Pert Pro) with an X-ray tube (Cu Kα, λ = 1.5406 Å). Steady-state PL spectra of the

perovskite films were recorded by using a fluorescent spectrophotometer (F-4600, HITACHI) with a 200 W Xe lamp as an excitation source. Absorption spectra were measured with a PerkinElmer model Lambda 900. The XRD patterns, UV and PL spectra for DDDA, ODEA and TTDDA treated perovskite films are shown in Supplementary Fig. 17. Similarly, we find no evidence for the formation of low dimensional perovskite within the resulting films from XRD, UV and PL measurements. The perovskite film morphology was characterized by the scanning electron microscope (SEM, LEO 1550 Gemini).

X-ray photoelectron spectroscopy (XPS) tests were carried out using a Scienta ESCA 200 spectrometer in ultrahigh vacuum (~ $1x10^{-10}$ mbar) with a monochromatic Al (K alpha) X-ray source providing photons with 1486.6 eV. The XPS experimental condition was set so that the full width at half maximum of the clean Au $4f_{7/2}$ line (at the binding energy of 84.00 eV) was 0.65 eV. All spectra were measured at a photoelectron take off angle of 0° (normal emission).

Time-of-flight secondary ion mass spectrometry (TOF-SIMS) tests were performed on a ToF-SIMS.5 instrument from IONTOF, Germany, operated in the spectral mode using a 25 keV Bi_3^+ primary ion beam with an ion current of 0.78 pA. A mass resolving power of ca. 6000 m/Δm was reached. For depth profiling a 1 keV Cs^+ sputter beam with a current of 39.81 nA was used to remove the material layer-by-layer in *interlaced mode* from a raster area of 500 × 500 µm. This raster area was chosen to ensure a flat crater bottom over an area of 100 × 100 µm used for the mass-spectrometry. The position of the ITO substrate interface in the sputter depth profile was defined by half maximum of the In_2^+ secondary ion count rate.

^{1}H Nuclear Magnetic Resonance (NMR). The ^{1}H NMR spectra were recorded on a Bruker Ultra Shield Plus 400 MHz NMR system. All the samples were prepared by dissolving 5 mg FAI in 0.4 ml dimethyl sulfoxide-d6 (DMSO-d6). For the blend samples, 15% EDEA or HMDA (molar ratio compared to FAI) was added.

Attenuated total reflectance-Fourier Transform Infrared (ATR-FT-IR). The ATR-FT-IR spectra were recorded from a PIKE MIRacle ATR accessory with a diamond prim in a Vertex 70 Spectrometer (Bruker) using a DLaTGS detector at room temperature. The measuring system was continuously kept in N_2

atmosphere. The spectra were acquired at 2 cm^{-1} resolution and 30 scans between 4000 and 800 cm^{-1}. The presented spectra were baselined-corrected by subtracting a linear baseline over the spectral ranges.

Aberration-corrected scanning transmission electron microscope (STEM). An FEI dual-beam FIB Helios workstation equipped with an in-situ micromanipulator and Pt gas injection system was used to prepare thin samples for STEM imaging. The final milling was performed at 3 kV. STEM investigations were conducted using JEOL ARM200F TEM equipped with a spherical aberration corrector at the condenser plane. A semi-convergence angle of 32 mrad was used. High-angle annual dark field (HAADF) and annual bright field (ABF) STEM were recorded with semi-angles in the range 68-280 mrad and 7-18 mrad, respectively.

Fluence-dependent PLQY and time-correlated single photon counting (TCSPC) measurements. The fluence-dependent PLQY was measured by a typical three-step technique with a combination of 445 nm continuous-wave (CW) laser, spectrometer, and an integrating sphere[42]. The TCSPC measurements were performed on an Edinburgh Instruments spectrometer (FLS980) with a 638 nm pulsed laser (less than 100 ps, 0.1 MHz). The total instrument response function (IRF) was less than 130 ps, and temporal resolution was less than 20 ps. All the perovskite films were deposited on ITO/ZnO:PEIE substrates with identical spin-casting condition for the optimized devices, and encapsulated by UV curable resin and glass slides.

Transient absorption (TA). The perovskite film samples were mounted in a chamber under dynamic vacuum ($<10^{-5}$ mbar). TA spectroscopy was conducted in transmission geometry. An amplified Ti:sapphire laser (Quantronix Integra-C) generated ~130 fs pulses centred at 800 nm, at a repetition rate of 1 kHz. A broadband white light probe was generated by focusing the pulses into a thin CaF_2 plate, and pump light at 400 nm was obtained via second harmonic generation in a BBO crystal. After interaction with the sample, a grating spectrometer was used to disperse the probe light on to a fast CCD array, enabling broadband shot-to-shot detection.

Trap density measurements by thermal admittance spectroscopy (TAS). For the device capacitance measurement, we used 0.4 M Pb^{2+} for all the cases to increase the signals. A sinusoidal voltage with a peek-to-peak value of 30 mV generated from a Tektronix AFG 3000 function generator was applied to the device.

The current signal of the devices was amplified with a SR570 low noise current preamplifier (Stanford Research Systems) and then analysed using a SR830 lock-in amplifier (Stanford Research Systems), where the amplitude and phase of the current can be measured. Based on the amplitude and phase of the current signal, the capacitance of the device was calculated using the parallel equivalent circuit model. The capacitance spectra of the device were measured by scanning the frequency of the sinusoidal voltage from 0.01 to 100 kHz in a logarithmic step. The temperature of the device was controlled using a DE202AE closed cycle cryocooler (Advanced Research Systems). The capacitance-voltage curve was obtained by measuring the capacitance when the applied DC bias voltage scanning from -0.5 to l.0 V. Based on the capacitance spectra measured at different temperature, the trap density (N_T) distribution in energy (E_ω) was calculated with the following relations:

$$N_T(E_\omega) = -\frac{V_{bi}}{qW}\frac{dC}{d\omega}\frac{\omega}{kT} \quad (2)$$

$$E_\omega = kT\ln\left(\frac{2\pi\nu_0 T^2}{\omega}\right) \quad (3)$$

where V_{bi} is the built-in potential, W is the depletion width, V_{bi} and W are derived from capacitance-voltage measurement, C is the capacitance measured at angular frequency of ω and temperature of T, k is the Boltzmann constant, ν_0 is the attempt-to-escape frequency, which can be obtained by fitting the relation of characteristic frequency with different T based on Equation (3).

Methods-only Reference

38. Bai, S. *et al.* High-performance planar heterojunction perovskite solar cells: Preserving long charge carrier diffusion lengths and interfacial engineering. *Nano Res.* **7,** 1749–1758 (2014).

39. Perdew, J. P., Burke, K. & Ernzerhof, M. Generalized gradient approximation made simple. *Phys. Rev. Lett.* **77,** 3865–3868 (1996).

40. Goedecker, S. & Teter, M. Separable dual-space Gaussian pseudopotentials. *Phys. Rev. B.* **54,** 1703–1710 (1996).

41. VandeVondele, J. & Hutter, J. Gaussian basis sets for accurate calculations on molecular systems

in gas and condensed phases. *J. Chem. Phys.* **127,** 114105 (2007).

42. De Mello, J. C., Wittmann, H. F. & Friend, R. H. An improved experimental determination of external photoluminescence quantum efficiency. *Adv. Mater.* **9,** 230–232 (1997).